

**CLOUD PARAMETER RETRIEVAL  
FROM COMBINED REMOTE SENSING OBSERVATIONS**

Jacques Testud\*, Claire Tinel, Anne Guyot and Karine Caillaud  
Centre d'études des Environnements Terrestres et Planétaires  
Vélizy, France

**1- INTRODUCTION**

To appreciate the radiative impact of clouds in the dynamics of the global atmosphere, it is important to deploy from space, from aircraft, or from ground, instruments able to describe the cloud layering and to document the cloud characteristics (namely liquid and/or ice water content, and the effective particle radius). Combining passive and active remote sensing techniques, microwave or VIS/IR, is a possible way to achieve this goal. Nevertheless, to build the inverse model and algorithms needed to retrieve the cloud parameters from remote sensing observations, a statistical knowledge of particle spectra drawn from microphysical data base is indispensable. The present paper covers three subjects:

- 1- Techniques to analyze particle spectra from cloud databases. What are the key parameters to characterize a particle spectrum? What is their statistics? How does they vary with temperature?
- 2- Building the inverse model. How the parameters which define the response of remote sensing instruments (radar reflectivity  $Z$ , radar specific attenuation  $K$ , lidar scattering coefficient  $\beta$ , lidar extinction coefficient  $\alpha$  relate to the cloud parameters interesting to evaluate cloud radiative properties (liquid water content LWC, ice water content IWC, effective radius of particles  $r_e$ ).
- 3- Algorithm retrieval. What are the uncertainties in the retrievals of radar or lidar alone? What brings combined observations of lidar and radar? What kind of combined algorithm can we consider to improve the retrieval?

---

\*Corresponding author: Jacques Testud,  
CETP-UVSQ, 10-12 avenue de l'Europe  
78140-Vélizy, France  
tel: 33(0)1 39 25 47 76; e-mail: [testud@cetp.ipsl.fr](mailto:testud@cetp.ipsl.fr)

**2- INVESTIGATING THE STATISTICAL PROPERTIES OF THE PSD**

The physical characterization of an observed cloud particle size distribution (PSD) raises three questions:

- (i) What liquid water content LWC (or ice water content IWC, if solid particles) corresponds to this PSD?
- (ii) What is the "mean" particle diameter?
- (iii) What is the "intrinsic" shape of the PSD?

The liquid water content relates to the cloud droplet size distribution  $N(D)$  [ $D$ : droplet diameter] as:

$$LWC = \frac{\pi \rho_w}{6} \int_0^{\infty} N(D) D^3 dD \quad (1)$$

where  $\rho_w$  is the density of water. The expression of the ice water content  $IWC$  is more complex since it depends on particle density and shape. We will use hereafter the formulation by Francis et al.(1998) who calculates the  $IWC$  from the microphysical observations as:

$$IWC = \frac{\pi \rho_w}{6} \int_0^{\infty} N(D_{eq}) D_{eq}^3 dD_{eq} \quad (2)$$

where  $D_{eq}$  is the "equivalent melted diameter", and  $N(D_{eq})$  is the PSD in equivalent melted diameter.  $D_{eq}$  is empirically related to the cross sectional  $A$  of the ice particle observed by the 2D probe through:

$$\begin{aligned} D_{eq} &= 1.097 A^{0.50}; & A \leq 0.0052 \text{ mm}^2 \\ D_{eq} &= 0.615 A^{0.39}; & A > 0.0052 \text{ mm}^2 \end{aligned} \quad (3)$$

The characterization of the mean particle size is more subjective. Ideally we should consider the effective particle radius  $r_e$  defined for a spectrum of liquid cloud droplets as:

$$r_e = \frac{3}{2} \frac{1}{\rho_w} \frac{LWC}{2A_c} = \frac{M_3}{2M_2} \quad (4)$$

where  $A_c$  is the integral of  $A$  over the PSD, and  $M_3$  and  $M_2$  are respectively the third and second moment of  $N(D)$ . However, for ice the effective radius is written as:

$$r_c = \sqrt{3}IWC / (3\rho_l A_c) \quad (5)$$

which cannot be expressed simply in terms of "moments" of  $N(D_{eq})$ .

In the following we prefer characterizing the mean particle size by the "volume weighted mean diameter" (usually referred to as the "mean volume diameter" in the literature) defined as:

$$D_m = M_4 / M_3 \quad (6)$$

where  $M_4$  and  $M_3$  denote the fourth and third moment of the PSD in  $D$  if liquid droplets, or in  $D_{eq}$  if ice particles.

Thus we defined the normalization of the PSD from the general form:

$$N(D) = N_0^* F(D/D_m) \quad (7)$$

where  $N_0^*$  is the normalization parameter along concentration axis,  $D_m$  the normalization parameter along diameter axis and  $F(X)$  is the "normalized PSD" describing the "intrinsic" shape of the PSD (noting  $X = D/D_m$ ). For an ice particle spectrum  $D$  stands for  $D_{eq}$ .

By virtue of (6),  $F(X)$  verifies:

$$\int_0^\infty F(X)X^4 dX = \int_0^\infty F(X)X^3 dX \quad (8)$$

While (1) [or (2) for an ice particle spectrum] provides:

$$\int_0^\infty F(X)X^3 dX = \frac{6}{\pi\rho_w} \frac{LWC}{N_0^* D_m^4} \quad (9)$$

In order to obtain a normalized function  $F$  independent of  $LWC$  and  $D_m$ , we should require that:

$$\int_0^\infty F(X)X^3 dX = C \quad (10)$$

where  $C$  is an arbitrary constant. A "natural" value to assign to the arbitrary constant  $C$  is  $C = 6/(\pi\rho_w)$ , such that the "normalized LWC" associated to the "normalized PSD" be equal to 1. However, we will show that this is not the best value for  $C$ , for the reason explained hereafter. It follows from (9) and (10) that  $N_0^*$  is defined by:

$$N_0^* = \frac{6}{C} \frac{1}{\pi\rho_w} \frac{LWC}{D_m^4} \quad (11)$$

When the PSD is an exponential of the form  $N(D) = N_0 \exp(-\Lambda D)$ , it may be easily shown that  $F(X) = \exp(-4X)$ , and that:

$$N_0^* = \frac{1}{C} N_0 \frac{\Gamma(4)}{4^4} \quad (12)$$

It is obviously interesting to define  $C$  such that  $N_0^*$  equals  $N_0$  when the PSD is exponential, thus  $C$  should be set to:

$$C = \Gamma(4) / 4^4 \quad (13)$$

and:

$$N_0^* = \frac{LWC}{\pi\rho_w} \frac{4^4}{D_m^4} \quad (14)$$

### 3- NORMALIZED PSD IN ICE CLOUDS OBSERVED DURING CLARE.

CLARE (Cloud and Radiation Experiment) deployed various observing systems for cloud and radiation at Chilbolton (England) in October 1998. The ground based experiment (including various meteorological radars and passive microwave observations) was coordinated with flights of three aircrafts: the C130 of the UK Met. Office, the Falcon of the German DLR, and the Fokker 27 "ARAT" of the French INSU. For the purpose of this paper, we are particularly interested in the C130 and Fokker 27 flights. The C130 performed microphysical sampling from 2DP, 2DC and FSSP probes in ice clouds at various altitude levels. The Fokker 27 was equipped with a cloud radar and a back-scattering lidar combination that provided the data exploited in section 6.

In this section we would like to report some results obtained from analyzing cloud ice particle spectra observed from the C130 using the approach described in section 2.

Fig. 1a&b show examples of normalized PSD obtained from ice particle spectra sampled at  $-32^\circ\text{C}$  and  $-9^\circ\text{C}$ , respectively. Each spectrum is integrated over 60s (i.e. 7.2 km). Note the remarkable stability of the PSD normalized shape between the various spectra collected at a given temperature. Meanwhile there is a significant difference in shape between  $-32^\circ\text{C}$  and  $-9^\circ\text{C}$ , which suggests to look for a model stratified in temperature.

At the opposite of this stability in shape, the normalization parameters  $N_0^*$  and  $D_m$  appear very variable and poorly correlated between themselves, as shown in the scatter plot of Fig.2.

In future work it would be essential to check if the stability of the shape of the PSD found for the CLARE data set maintains when our analysis is applied to others data sets (with different cloud types, corresponding to different climatic zones, etc.). A key point in particular would be to check if the temperature suffices to define the shape of the normalized PSD.

### 4- INVERSE MODEL FOR RADAR AND LIDAR RETRIEVAL

Moments of the DSD represent more or less faithfully most of the integral parameters of the DSD interesting in for radar or lidar data analysis. This is the reason for this investigation of the relationships between moments. A general expression of the  $i^{\text{th}}$  order moment of the DSD is:

$$M_i = \int N_0^* F(D/D_m) D^i dD = N_0^* D_m^{i+1} \xi_i \quad (15)$$

where  $\xi_i$  is the  $i^{\text{th}}$  order moment of the normalized distribution  $F(X)$ :

$$\xi_i = \int F(X) X^i dX \quad (16)$$

Thus, between two moments of order  $i$  and  $j$ , the following relationship stands:

$$\frac{M_i}{N_0^*} = \xi_i \xi_j^{-\frac{i+1}{j+1}} \left[ \frac{M_j}{N_0^*} \right]^{\frac{i+1}{j+1}} \quad (17)$$

$$M_i = \xi_i \xi_j^{-\frac{i+1}{j+1}} [N_0^*]^{\frac{i+1}{j+1}} M_j^{\frac{i+1}{j+1}} \quad (18)$$

Equations (17) and (18) establish that, when parameterized by  $N_0^*$ , the relationship between two moments of order  $i$  and  $j$  of the DSD is a power law whose exponent is  $(i+1)/(j+1)$ . Equation (17) also shows that after normalization of the moments by  $N_0^*$ , the power law relationship only depends on the moments of  $F(X)$ . Indeed such a dependence is expected to be weak (as far as realistic  $F(X)$ 's are considered), since by definition  $\xi_3 = \xi_4 = \Gamma(4)/4^4$ , which strongly constrains the other moments. The same argument may be used to emphasize [from (18)] the fact that the variability of the relationship between two moments is mainly due to that in  $N_0^*$  which appears to be a key parameter of the relationship between moments.

The above equations (1) to (5) show how the "physical" parameters interesting to appreciate the effect of the cloud on the radiative budget of the atmosphere,  $LWC$  (or  $IWC$ ) and  $r_e$ , relate to moments of the PSD. Similarly the equivalent radar reflectivity  $Z_e$ , the specific radar attenuation  $K$ , the backscattering coefficient for lidar  $\beta$ , the lidar extinction coefficient  $\alpha$ , are approximately proportional to moments of the PSD. For a spectrum of liquid cloud droplets, we have simply, in the framework of the Rayleigh approximation:

$$Z_e = M_6 \quad (19)$$

For a spectrum of ice particles, and with the same Rayleigh approximation,  $Z_e$  expresses as:

$$Z_e = \frac{|K_i|^2}{\rho_i^2 |K_w|^2} M_6 \quad (20)$$

where  $K_i$  and  $K_w$  are the refractive coefficients for ice and water, respectively, and  $\rho_i$  is the density of solid ice.

The radar attenuation  $K$  is approximately proportional to a moment of order between 3 and 4 following the type of particles (liquid or solid) and their size (validity of the Rayleigh approximation).

The lidar extinction coefficient  $\alpha$  is approximately given by:

$$\alpha = 2A_c \quad (21)$$

Thus  $\alpha$  is proportional to  $M_2$  for liquid particles, and to a moment of order approximately 2.5 for ice particles.  $\beta$  is proportional to  $\alpha$ :

$$\beta = f\alpha \quad (22)$$

with coefficient  $f$  depending on particle shape and orientation.

For a given shape  $F(X)$  of the normalized PSD, we expect from (17) that the relationship between two integral parameters of the PSD, after normalization by  $N_0^*$ , be functional. As we have seen in section 3, that is not exactly true: systematic variation of the shape are observed as a function of the temperature. Despite this fact, Figs. 3 a,b&c show that for the CLARE data set, the normalized relationships between  $K$  and  $Z_e$ ,  $\alpha$  and  $K$ ,  $IWC$  and  $K$  are almost functional. This demonstrates the robustness of our Inverse Model, funded upon the following set of power-laws relationships [together with (22)]:

$$K = a [N_0^*]^{-b} Z_e^b \quad (23)$$

$$\alpha = c [N_0^*]^{-d} K^d \quad (24)$$

$$IWC = p [N_0^*]^{-q} K^q \quad (25)$$

## 5- CLOUD RADAR AND LIDAR SYNERGETIC ALGORITHM

### 5.1- Similarity of the inversion problem for radar and lidar

The radar measures an apparent (attenuated) radar reflectivity defined as:

$$Z_a = Z_e \cdot 10^{0.2 \int_0^r K(s) ds} \quad (26)$$

Under the assumption of a power-law between  $K$  and  $Z_e$ , (26) may be inverted to retrieve  $Z_e$ . Hitschfeld, and Bordan gave the exact solution of this inversion in 1954 [hereafter referred to as HB54]. However, as recognized by these authors, this solution is numerically unstable, unless an external constraint be

integrated in the process. One of the reasons of this instability is the impossibility to set a fixed relationship between  $K$  and  $Z_e$  because of the natural variability of  $N_0^*$ .

Similarly, the lidar measures an apparent back-scattering coefficient  $\beta_a$  defined as:

$$\beta_a = \beta \cdot \exp \left[ -2 \int_0^r \alpha(s) ds \right] \quad (27)$$

If it is assumed that  $\beta$  and  $\alpha$  are related through a relation like  $\beta=f\alpha$ , the problem posed by the inversion of (27) for  $\beta$  is formally identical to that solved by HB54, as recognized by Klett (1981). The numerical instability of the solution, and the necessity of an external constraint are the same.

Various possibilities have been investigated for the external constraint. For example, with the TRMM precipitation radar, the external constraint is found in an estimate of the integrated path attenuation between the satellite and the ocean surface, used as a reference target. With the lidar, the molecular scattering measured beyond the cloud layer provide the reference target. What we want to investigate presently is a combined constraint between the cloud radar and the lidar.

### 5.2- A combined radar and lidar algorithm

The HB54 solution of (26) may be written with respect to  $K$  in the following manner (Testud et al., 2000):

$$K(r) = \frac{K(r_0)Z_a^b(r)}{Z_a^b(r_0) + 0.46bK(r_0)\int_r^{r_0} Z_a^b(s)ds} \quad (28)$$

where  $r_0$  is a reference bound ( $r < r_0$ ).

The interest of such a formulation is that (i) it eliminates the very variable  $N_0^*$  parameter, and (ii) it provides an expression of the  $K$  profile not subject to radar calibration uncertainty. However the value at the reference bound  $K(r_0)$  has to be determined independently.

In the same way, the Klett solution of (27) may be written as:

$$\alpha(r) = \frac{\alpha(r_0)\beta_a(r)}{\beta_a(r_0) + 2\alpha(r_0)\int_r^{r_0} \beta_a(s)ds} \quad (29)$$

Here the expression of  $\alpha(r)$  is independent from  $f$  and from the lidar calibration, but is subject to the determination of  $\alpha$  at the reference bound  $r_0$ .

To determine  $K(r_0)$  and  $\alpha(r_0)$  in (28) and (29), we use the following integral constraint:

$$\int_{r_1}^{r_0} \alpha(s)ds = c[N_0^*]^{-d} \int_{r_1}^{r_0} K^d(s)ds \quad (30)$$

This integral constraint expresses the consistency of  $K(r)$  and  $\alpha(r)$  profiles with relationship (24) of the Inverse Model. The bounds of integration  $r_1$  and  $r_0$  should be chosen such that the type of particles is the same along  $[r_1, r_0]$  in order to legitimate the implicit assumption made in (28) and (29) that  $N_0^*$  and  $f$ , respectively, are constant along the path. Since  $\alpha(s)$  and  $K(s)$  in (30) are function of  $\alpha(r_0)$  [ $\alpha(s)$  through (29), and  $K(s)$  through (28) and (24)], (30) may be considered as an implicit equation in  $\alpha(r_0)$  that may be solved by a standard numerical technique. Once  $\alpha(r_0)$  has been determined, then the  $K$  and  $\alpha$  profiles between  $r_1$  and  $r_0$  may be derived, and subsequently  $IWC$  and  $r_c$  through (25), (21) and (5). Nevertheless the difficulty to overcome is related to the presence of parameter  $N_0^*$  in (30). The way to get around is to start with a first guess

of  $N_0^*$ , then to determine the  $K$  and  $\alpha$  profiles, then to derive an improved estimate of  $N_0^*$  as in Testud et al. (2000) through:

$$N_0^* = \left[ \frac{1}{a Z_a(r_0) + K(r_0)I(r_1, r_0)} \right]^{\frac{1}{1-b}} \quad (31)$$

$$\text{where } I(r_1, r_0) = 0.46b \int_{r_1}^{r_0} Z_a^b(s)ds$$

This estimate may be used in (30) to restart the process. The convergence is generally met in a few iterations. The algorithm also provides an estimate of  $f$  (assumed constant along the segment  $[r_1, r_0]$ ) as:

$$f = \frac{\beta_a(r_0)}{\alpha(r_0)} + 2 \int_{r_1}^{r_0} \beta_a(s)ds \quad (32)$$

The above-described algorithm has several advantages:

- (i) it does not need to specify any value for  $f$  (though  $f$  is assumed constant along  $[r_1, r_0]$ );  $f$  is estimated by the algorithm;
- (ii) it calculates parameter  $N_0^*$  that scales all the relationships of the inverse model;
- (iii) it can be segmented according to the various cloud layers met on the path, allowing to adjust a distinct  $N_0^*$  for the different layers.

However it should be noticed that the  $N_0^*$  estimate given in (31) is dependent on the radar calibration. Thus though the  $K$  profile from (28) is free from radar calibration error, the algorithm requires a good radar calibration.

## 6- APPLICATION OF THE SYNERGETIC ALGORITHM REAL DATA

In CLARE the ARAT was equipped with the nadir looking "LEANDRE" lidar operating at 0.5  $\mu$  developed by Service d'Aéronomie and INSU, and with the 95 GHz cloud radar of University of Wyoming, connected to the dual beam antenna of CETP (looking alternately at nadir and at 45° fore).

The synergy between radar and lidar is particularly efficient when probing an ice cloud, since the penetration of the radar and of the lidar in this type of cloud is comparable. The subsequent data analysis is focused on a particular leg [20 October 1998 from 14:41 to 14:48] where the ARAT was flying around 4.4 km altitude, and the C130 was flying at 4.6 km altitude along the same leg. The altitude of the freezing level was around 1.8 km. Thanks to a good coordination between the two aircrafts, a very satisfactory coincidence in space and time of the ground tracks of the two aircrafts was met on this leg. Between longitudes 1.7 and 2°W and above 3 km altitude, the two instruments (nadir looking) really see the same cloud, and the synergetic algorithm can be efficiently performed. The Inverse Model considered

in the retrieval is the following, corresponding to Figs.3 a,b&c:

$$\begin{aligned} K &= 2.7758 \times 10^{-5} N_0^{*0.3288} Z^{0.6712} \\ \alpha &= 0.1485 N_0^{*0.3056} K^{0.6944} \\ IWC &= 6.994 \times 10^{-2} N_0^{*0.2149} K^{0.7851} \end{aligned} \quad (33)$$

Figs. 4 and 5 show examples of retrieved profiles of  $Z_e$ ,  $\alpha$ ,  $IWC$  and  $r_e$ , at 1.75°W and 1.80°W. Fig. 6 displays the along track evolution of the parameters retrieved by the synergetic algorithm [ $Z_e$ ,  $\alpha$ ,  $IWC$ ,  $r_e$ , and  $N_0^*$ ] at the highest altitude observable with the cloud radar and lidar: 4.3 km altitude. Fig.6 also shows the along track evolution of  $IWC$ ,  $r_e$  and  $N_0^*$  deduced from the C130 microphysical probes at 4.6 km altitude. The agreement between the radar/lidar retrieval and the microphysical probes is rather good between longitudes 1.67°W and 1.84°W, particularly for  $IWC$ . Beyond 1.84° longitude the synergetic algorithm diverges because the penetration of the lidar is insufficient.

## 7- CONCLUSION

From these first tests with from the CLARE data set, the potential of the cloud radar and lidar combination on the

same platform seems very promising. Further analysis should be directed towards:

- (i) extending the analysis to other microphysical data sets to test the degree of generality of the inverse model;
- (ii) investigate the segmentation of the analysis in the conditions where different types of cloud are met along the beam.

## References

- Francis et al.,1998:  
 Hitschfeld, W., and J. Bordan, 1954: Errors inherent in the radar measurement of rainfall at attenuating wavelengths. *J. Meteor.*, 11, 58-67.  
 Klett J.D., 1981, Stable Analytical Inversion Solution for Processing Lidar Returns, *20*, 2, 211-220.  
 Testud J., E. Le Bouar, E. Obligis, M. Ali Mehenni, 2000: The rain profiling algorithm applied to polarimetric weather radar, *Jour. of Atmosph. and Oceanic Technol.* **17**, No 3, 332-356.

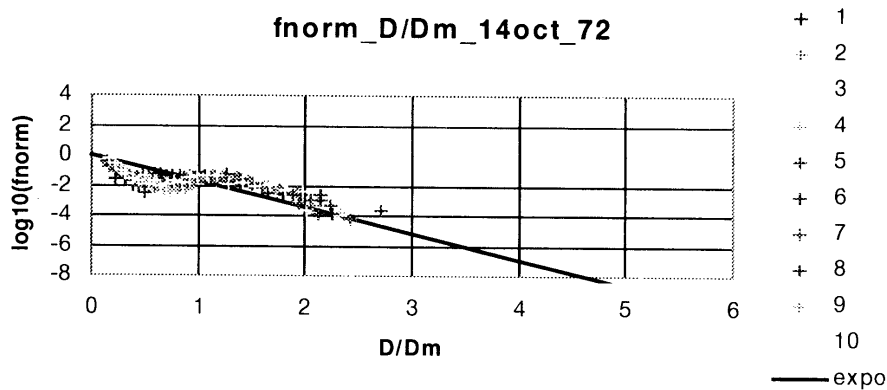


**Fig.1a:** The Normalized PSD for the legs of CLARE at -32°C temperature.

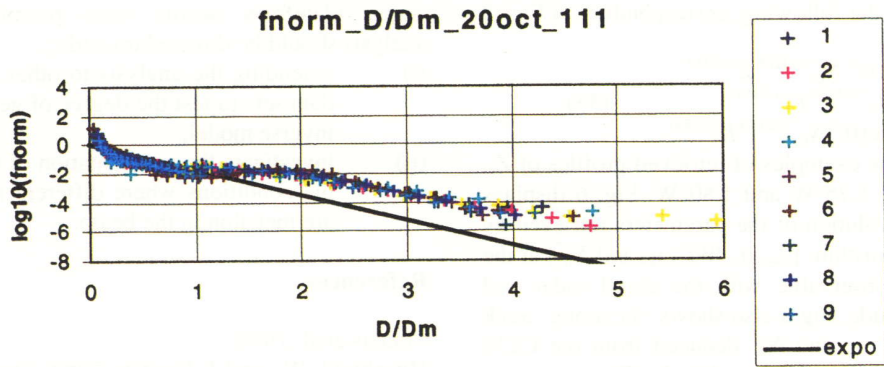


Fig.1b: The Normalized PSD for the legs of CLARE at  $-9^{\circ}\text{C}$  temperature.

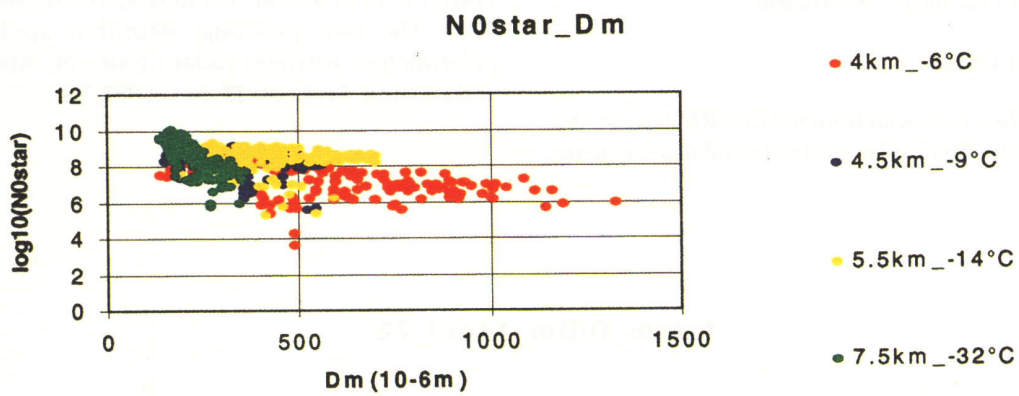


Fig. 2: Scatter plot of  $N_0^*$  versus  $D_m$  for the CLARE microphysical data set

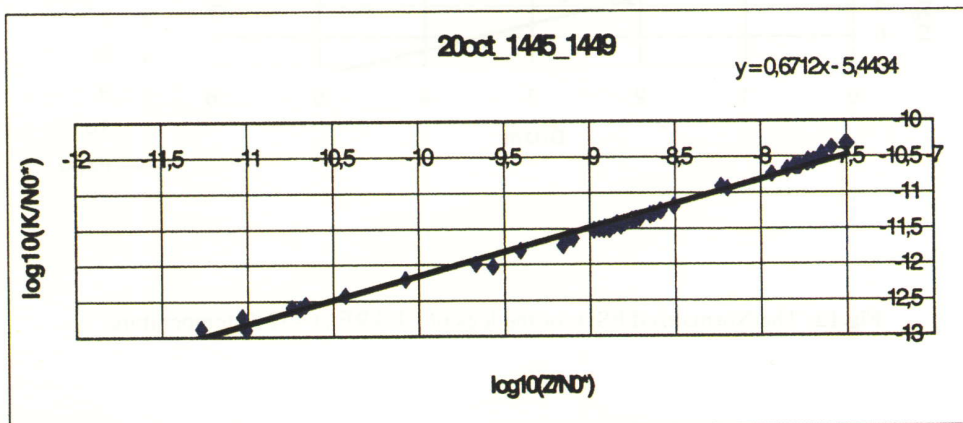
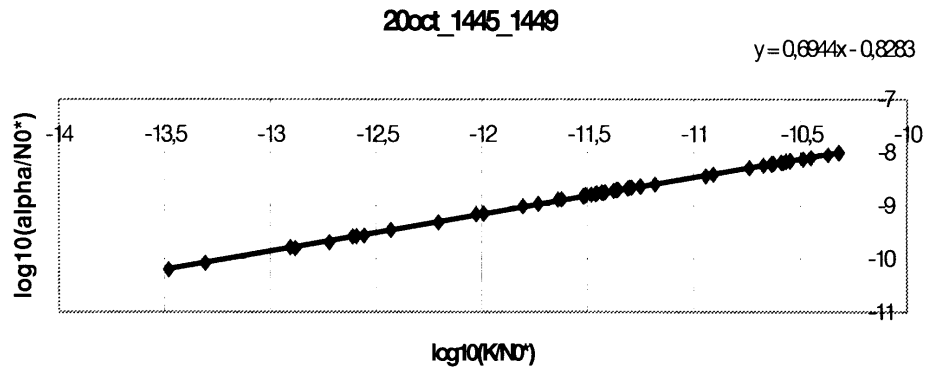
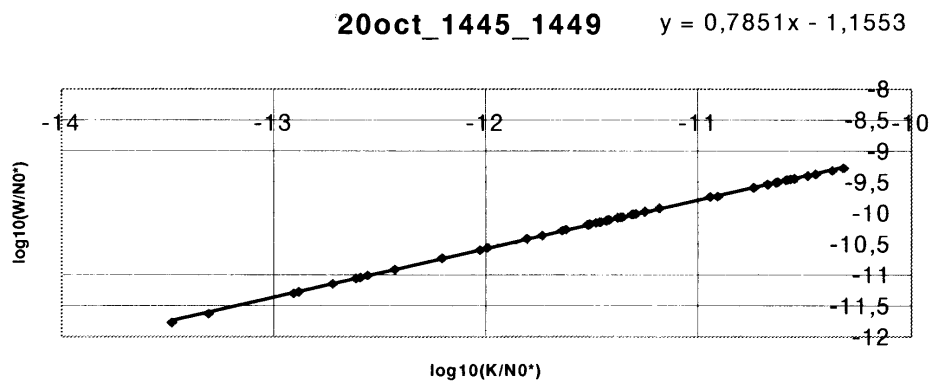


Fig. 3a: The  $K/N_0^*$  versus  $Z_d/N_0^*$  relationship for the CLARE microphysical data set and for a 95GHz radar



**Fig. 3b:** The  $\alpha/N_0^*$  versus  $K/N_0^*$  relationship for the CLARE microphysical data set and for a 95GHz radar



**Fig. 3c:** The  $IWC/N_0^*$  versus  $K/N_0^*$  relationship for the CLARE microphysical data set and for a 95GHz radar

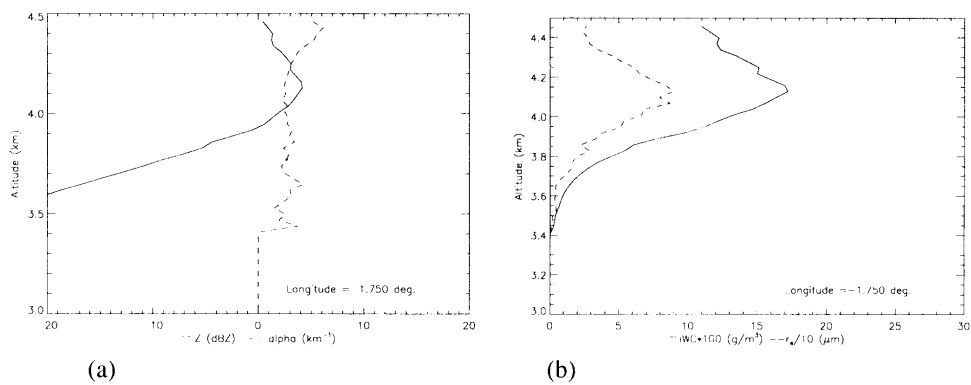


**Fig. 4:** Illustration of the profiles of  $Z_e$  and  $\alpha$  [in(a)] and  $IWC$  and  $r_e$  [in (b)] retrieved by the synergetic algorithm (longitude along aircraft track: 1.75°W)

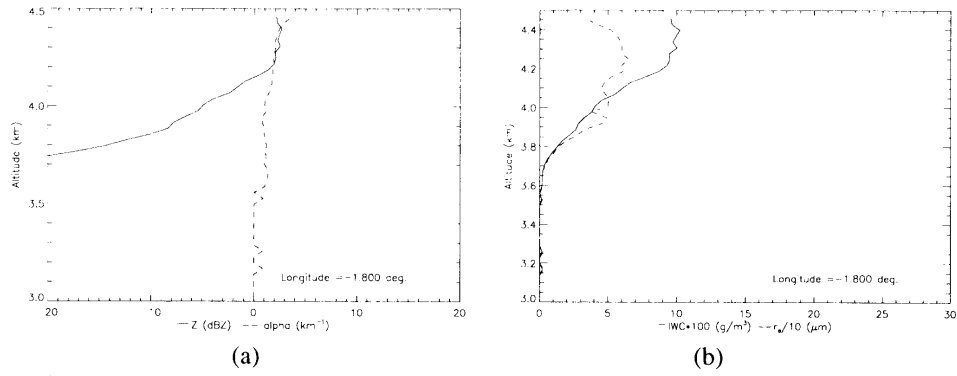


**Fig. 5:** Illustration of the profiles of  $Z_e$  and  $\alpha$  [in (a)] and  $IWC$  and  $r_e$  [in (b)] retrieved by the synergetic algorithm (longitude along aircraft track:  $1.8^\circ\text{W}$ )

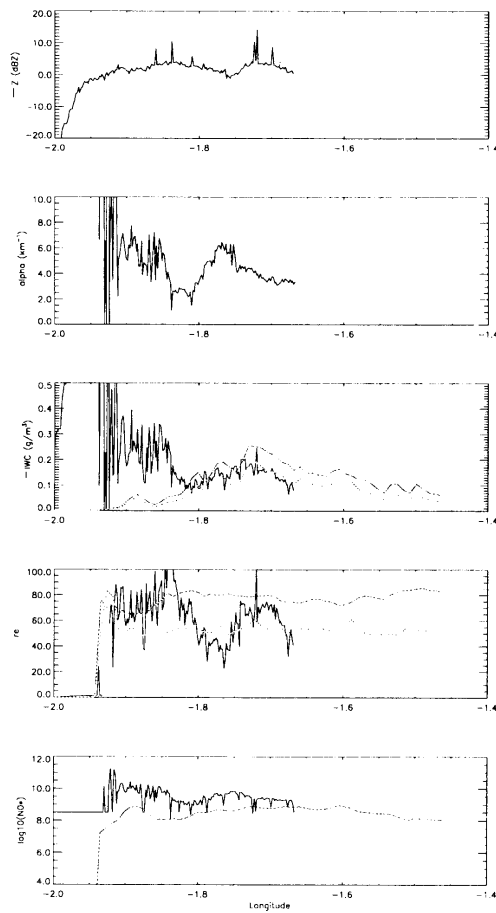


**Fig. 6:** Along track evolution at 4.3 km altitude of the various parameters retrieved from the synergetic algorithm. From top to bottom: radar reflectivity  $Z_e$ , extinction coefficient  $\alpha$ , ice water content  $IWC$ , effective radius  $r_e$ , PSD parameter  $N_0^*$ . The last three are compared with the estimates derived from the CI30 microphysical data at 4.6 km altitude. Note for longitude beyond  $1.85^\circ\text{W}$  the collapse of the algorithm due to insufficient penetration of the lidar.